Catalysis Today 160 (2011) 87–95

Contents lists available at ScienceDirect

Catalysis Today

journal homepage: www.elsevier.com/locate/cattod

Heterostructured catalysts prepared by dispersing Au@Fe_2O_3 core–shell structures on supports and their performance in CO oxidation

Hongfeng Yin[a], Zhen Ma[b], Miaofang Chi[c], Sheng Dai[a,*]

[a] Chemical Sciences Division, Oak Ridge National Laboratory, Oak Ridge, 1 Bethel Valley Road, TN 37831, USA
[b] Department of Environmental Science and Engineering, Fudan University, Shanghai 200433, PR China
[c] Materials Science and Technology Division, Oak Ridge National Laboratory, Oak Ridge, TN 37831, USA

ARTICLE INFO

Article history:
Available online 12 June 2010

Keywords:
Gold
Fe_2O_3
Au@Fe_2O_3
Core–shell
Nanoparticles
Catalysis
CO oxidation

ABSTRACT

Herein, we report novel gold catalysts made by dispersing Au@Fe_2O_3 core–shell structures on solid supports. In the synthesis of Au@Fe_2O_3 core–shell structures, dodecanethiol-capped gold nanoparticles were used as the seed and $Fe(CO)_5$ was used as the precursor to Fe_2O_3 shell. The Au@Fe_2O_3 core–shell particles were deposited onto SiO_2 support to obtain Au@Fe_2O_3/SiO_2 catalysts that were highly active for low-temperature CO oxidation. The catalytic activity was even higher than that of Au/SiO_2 or Au/Fe_2O_3 prepared by colloidal deposition with comparable gold loadings. The influences of thermal pretreatment, shell thickness, and different supports (e.g., SiO_2, TiO_2, C, Fe_2O_3) were investigated, and relevant characterization using TG/DTG, XRD, TEM, HAADF, and EDX was conducted.

1. Introduction

Gold nanoparticles dispersed on solid supports have many potential applications in environmental catalysis, chemical synthesis, and clean energy processing [1–8]. These catalysts are usually prepared by deposition–precipitation and colloidal-deposition [9–19] methods and the supports often used are TiO_2, CeO_2, Fe_2O_3, Al_2O_3, ZrO_2, SiO_2, and C. More complicated gold catalysts may be desirable for achieving better performance and stability in catalysis [20–30]. Along this line, our group has previously explored the use of Au–Fe_3O_4 dumbbell heterostructures on SiO_2, TiO_2, and C supports to stabilize gold nanocatalysts and demonstrated the high activities and thermal stability of these catalysts in CO oxidation [31]. We have also dispersed colloidal NiAu particles onto SiO_2 supports and demonstrated that upon oxidative pretreatment at elevated temperatures, NiAu nanoparticles could transform into Au nanoparticles whose surfaces were decorated by amorphous NiO [32,33]. This Au–NiO/SiO_2 catalyst was active for low-temperature CO oxidation. In the current contribution, we report the application of Au@Fe_2O_3 core–shell structures [34] as the precursor for the preparation of supported catalysts highly active for low-temperature CO oxidation (Scheme 1).

Great effort has been made toward the designing of metal@oxide core–shell structures [34–39]. However, only limited attention has been paid to the use of core–shell structures [40–49] or their supported versions [49–52] in making new catalysts [53,54]. Notably, Tsang and co-workers prepared a CeO_2-encapsulated-Pt catalyst (denoted as Pt@CeO_2) via a microemulsion method [43,44]. The catalyst showed activity in water–gas shift reaction comparable to Cu/ZnO and Pt/CeO_2 catalysts, and there was no formation of undesirable methane. In another work, Tsang and co-workers prepared a Pt@SiO_2/Al_2O_3 catalyst for the hydrogenation of toluene [52]. The resulting catalyst showed much higher thermal stability than Pt/SiO_2–Al_2O_3. More recently, Somorjai and co-workers designed Pt@SiO_2 core–shell structures for CO oxidation [47]. This catalyst had not only mesopores caused by the removal of residual organic species, but also good thermal stability due to the presence of SiO_2 shell.

Little effort has been paid to the use of Au@oxide core–shell structures in catalysis. Others have prepared new catalysts featured by the strategic location of small gold nanoparticles in much bigger hollow ZrO_2 or SiO_2 shells [55–58] or by the entrapment of a number of gold nanoparticles in amorphous SiO_2 matrix [59]. These catalysts showed enhanced thermal stability due to the encapsulation of gold nanoparticles in inorganic matrixes. Recently, Xie and co-workers synthesized Au@SnO_2 core–shell structures by an intermetallics-based dry-oxidation approach [60]. There were several steps in their approach: (1) Gold nanoparticles were prepared by reducing $HAuCl_4$ by a sodium citrate solution; (2) AuSn nanoparticles were prepared by reducing $SnCl_2$ by $NaBH_4$ in the presence of the pre-synthesized gold nanoparticles; (3) The Au@SnO_2 core–shell structure was formed via a three-step oxida-

* Corresponding author.
E-mail address: dais@ornl.gov (S. Dai).

0920-5861/$ – see front matter © 2010 Elsevier B.V. All rights reserved.
doi:10.1016/j.cattod.2010.05.013

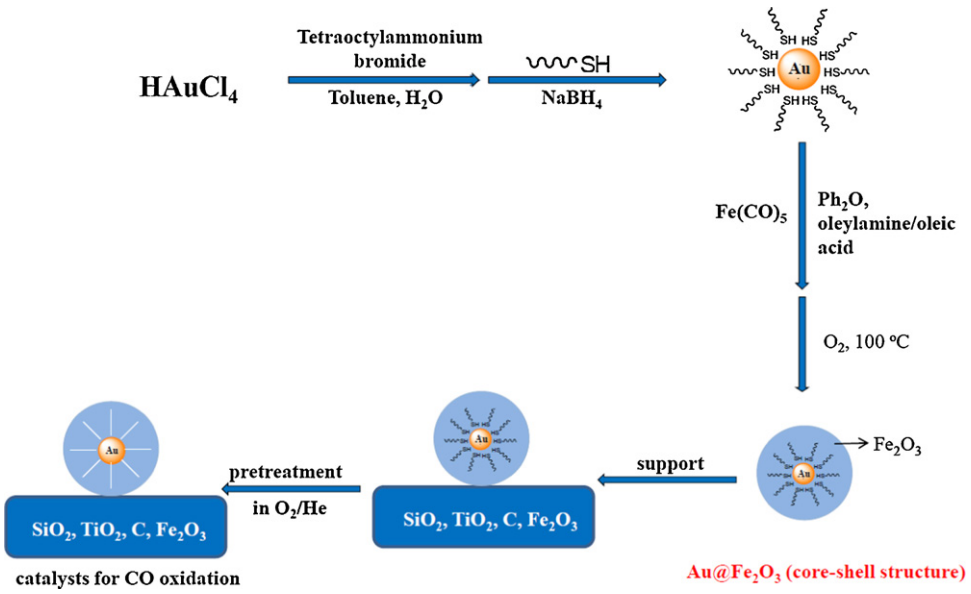

Scheme 1. Preparation of supported Au@Fe_2O_3 nanoparticles.

tion procedure. As a result, gold nanoparticles with a mean size of 15 nm were encapsulated by the SnO_2 shell with a thickness of 6–7 nm. The core–shell structured catalyst still showed 50% CO conversion when the reaction temperature was 230 °C, even though the catalyst was pretreated at 850 °C prior to reaction testing. The authors proposed that the relatively high activity of Au@SnO_2 was due to a synergetic confinement effect, the electron transfer from the oxide support to gold nanoparticles, and larger interaction areas [60]. Nevertheless, the size of gold nanoparticles was still too big for catalysis, and the preparation method was relatively complicated. In another work, Xu and co-workers synthesized bimetallic Au–Ni nanoparticles embedded in SiO_2 spheres, and demonstrated that Au–Ni@SiO_2 showed higher catalytic activity and better durability than monometallic Au@SiO_2 and Ni@SiO_2 in the hydrolysis of ammonia borane [48].

In this contribution, we designed supported Au@Fe_2O_3 catalysts and tested their activity in CO oxidation. We have chosen Fe_2O_3 as the shell based on below considerations. First, the synthesis of Au@Fe_2O_3 has been established in the materials community [34]. Second, Au/Fe_2O_3 with Au–Fe_2O_3 interface is known to be active in CO oxidation [61–67]. Therefore, we expect that supported Au@Fe_2O_3 catalysts should also be active in CO oxidation. We are interested in investigating the following questions. First, is there any requirement for catalyst pretreatment in order to obtain high catalytic activity? Second, what is the effect of shell thickness on catalytic activity? Third, what effect can be induced if the underlying support is different? Finally, how do supported Au@Fe_2O_3 catalysts compare to Au/SiO_2, Au/TiO_2, Au/C, Au/Fe_2O_3, and Au@Fe_2O_3? The results from our work provide insights for the preparation and application of supported gold core-oxide shell catalysts.

2. Experimental

Gold nanoparticles were synthesized according to a classic method [68–70]. $HAuCl_4 \cdot 3H_2O$ (0.63 g) was added into 50 mL deionized water, and the aqueous solution was added, with vigorous stirring, into a solution containing 3.0 g tetraoctylammonium bromide and 160 mL toluene. The yellow $HAuCl_4$ solution became clear quickly and the toluene phase became orange-brown as the gold precursor was transferred into it. The organic phase was isolated, 80 mg dodecanethiol was added, and the resulting solution was stirred at room temperature for 10 min. $NaBH_4$ (0.72 g) in 50 mL deionized water was added in 10 s, with vigorous stirring. The dark organic phase was stirred at room temperature for 3 h. The organic phase was collected, and the solvent was evaporated with the aid of a rotary evaporator (not exceeding 50 °C to avoid product decomposition). The black product was dispersed into 30 mL acetone, sonicated to ensure complete dissolution, and precipitated by adding 80 mL ethanol. The product was washed with hexane/ethanol for 3 times and dried in a vacuum oven at room temperature for 10 h, yielding sticky black solid. The resulting gold nanoparticles have an average size of 2.1 nm, as estimated by XRD measurement of gold nanoparticles supported on SiO_2.

Au@Fe_2O_3 core/hollow-shell NPs were synthesized with a modified method [71]: 3 mL toluene solution containing 22 mg gold nanoparticles was sonicated for 5 min. Then 50 mL diphenyl ether and 0.3 mL oleylamine–oleic acid mixture (1:1 in volume) were added to the flask, and the mixture was stirred for 5 min followed with sonication for 5 min. The solution was kept under vacuum at 80 °C for 30 min, and then the solution was purged with N_2 at room temperature for 10 min before 0.3 mL $Fe(CO)_5$ was injected into solution and kept at 200 °C for 30 min. The solution was cooled to 100 °C, and air was passed through the solution for about 10 min. The resulting mixture was washed with hexane–ethanol solvent–nonsolvent combination followed by centrifugation. The dark-red precipitate was dispersed in 30 mL hexane to obtain colloidal Au@Fe_2O_3 sample. TEM characterization revealed that the Fe_2O_3 thickness of Au@Fe_2O_3 was around 2 nm, and this sample is denoted as Au@Fe_2O_3-II. Au@Fe_2O_3-I, Au@Fe_2O_3-III, and Au@Fe_2O_3-IV samples with Fe_2O_3 thickness estimated to be about 1, 3, and 4 nm were synthesized using the same procedure except that the amount of $Fe(CO)_5$ used was 0.12, 0.8, and 1.6 mL, respectively, and the amount of oleylamine–oleic acid mixture was 0.3, 0.6, and 1.2 mL, respectively.

Au@Fe_2O_3/support samples were prepared via direct colloidal deposition. Colloidal Au@Fe_2O_3 (10 mL) obtained above was dispersed into 30 mL hexane and stirred for 10 min, followed with the addition of 0.18 g SiO_2 (Cab-O-Sil, surface area 175 m^2/g), TiO_2 (Degussa P25, surface area 48 m^2/g), carbon (carbopack, surface area 165 m^2/g), or α-Fe_2O_3 (Aldrich, surface area 10 m^2/g). The suspension was stirred vigorously for 1 h and stirred slowly in open

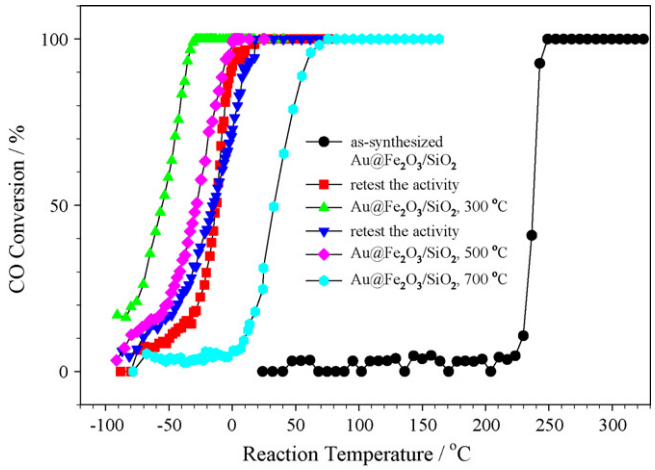

Fig. 1. CO conversions on $Au@Fe_2O_3/SiO_2$ either not pretreated or pretreated at different temperatures (300, 500, or 700 °C). The thickness of the original Fe_2O_3 shell was estimated to be 2 nm.

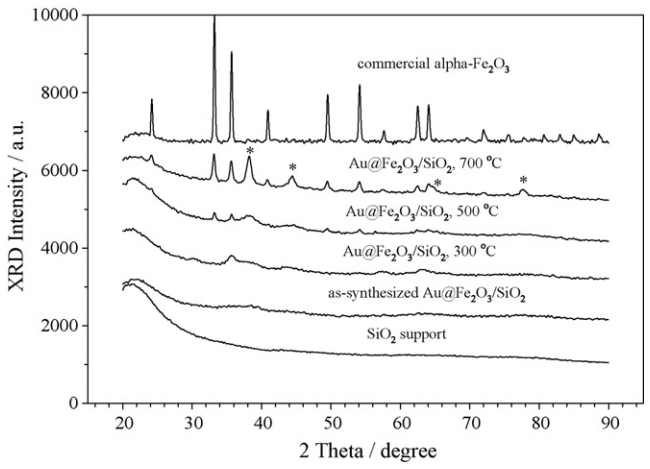

Fig. 2. XRD patterns of $Au@Fe_2O_3/SiO_2$ either not pretreated or pretreated at different temperatures (300, 500, or 700 °C) and subjected to reaction testing. The thickness of the original Fe_2O_3 shell was estimated to be 2 nm. A commercial α-Fe_2O_3 was used as for comparison. The peaks corresponding to metallic gold were marked with star.

air for the evaporation of solvent. The remaining solid was washed with ethanol (2 × 20 mL) and dried under vacuum at 60 °C for 10 h.

For comparison, Au/support samples were prepared by colloidal deposition. Gold nanoparticles (20 mg) were dispersed into 30 mL hexane and stirred for 10 min, followed by the addition of 0.5 g SiO_2, TiO_2, C, or α-Fe_2O_3. The suspension was stirred vigorously for 1 h and stirred slowly in open air to evaporate the solvent. The remaining solid was dried in a vacuum oven at 60 °C for 10 h. The intended gold loading was 4 wt%, and the actual gold loadings of samples were measured by EDX as 3.3–3.8 wt% (Table 1).

Unless otherwise specified in the text, a 50 mg sample was packed into a U-type quartz tube (i.d. = 4 mm) sealed by quartz wool and pretreated in flowing 8% O_2 (balance He) at a specified temperature for 1 h (heating rate, 30 °C/min; flow rate, 37 cm^3/min). After cooling, a gas stream of 1% CO (balance air, <4 ppm water) flowed through the catalyst at a rate of 37 cm^3/min, and the exiting stream was analyzed by a gas chromatograph equipped with a dual molecular sieve/porous polymer column and a thermal conductivity detector. The reaction temperature was varied using a furnace or by immersing the U-type tube in ice–water or liquid N_2 cooled acetone.

TG/DTG experiments were conducted on a TGA 2950 instrument using a heating rate of 10 °C/min under N_2 or air atmosphere. XRD data were collected on a Siemens D5005 diffractometer with Cu Kα radiation, in the range of 2θ = 20–90° at the rate of 0.01°/s. TEM experiments were carried out on a Hitachi HD-2000 STEM operated at 200 kV. High angle annular dark field (HAADF)–STEM images were obtained using an aberration-corrected FEI Titan 80/300-kV TEM/STEM with a convergence angle of 16.8 mrad and a large inner collection angle of 55 mrad. The images were acquired at "fresh" sample area without pre-electron beam irradiation. EDX experiments were conducted on a JEOL JSM-6060 scanning electron microscope coupled with an EDX detector.

3. Results and discussion

3.1. Case study of $Au@Fe_2O_3/SiO_2$: effect of pretreatment temperature

Fig. 1 shows the light-off curves of $Au@Fe_2O_3/SiO_2$ catalysts under different pretreatment conditions. The thickness of the Fe_2O_3 shell is estimated as 2 nm, as described in Supporting Information. The as-synthesized $Au@Fe_2O_3/SiO_2$ catalyst is not active for CO oxidation when the reaction temperature is below 200 °C. The conversion increases sharply in between 230 and 250 °C, and the T_{50} (temperature required for 50% CO conversion) value is 238 °C. After the catalytic test was finished, we repeated the activity testing by cooling the spent catalyst and increasing the reaction temperature again. Interestingly, the spent catalyst is now much more active (T_{50} = 12 °C). This observation indicates that the observed activation phenomenon is due to the combustion and desorption of organic species when the reaction temperature is ramped in the first run [72]. To further verify this conjuncture, we pretreated a fresh as-synthesized $Au@Fe_2O_3/SiO_2$ catalyst at 300 °C prior to reaction testing and found that the 300 °C-pretreated catalyst (T_{50} = −55 °C) is much more active than the as-synthesized catalyst without pretreatment (T_{50} = 238 °C). Our TG/DTG data in Fig. S1 also indicate the weight loss corresponding to the desorption of water and removal of residual organic species, respectively. The removal of organic species is more efficient in air (right panel) than in N_2 (left panel). Therefore, it is necessary to pretreatment the catalysts in order to remove residual organic species [12,13,15,17–19,59,73–78].

Fig. 1 also indicates that the catalytic activity decreases when the catalyst is pretreated at 500 or 700 °C (T_{50} = −28 and 33 °C, respectively), although these two catalysts show significant CO conversions below room temperature. To compare the activity more quantitatively, specific rates were calculated based on the CO concentration (1 mol%), flow rate (37 ml/min), CO conversions at −40 °C read from the conversion curves, the amount of catalyst put into the reactor (50 mg), and gold loading (3.3 wt% Au) measured by EDX (Table 1). For instance, the CO conversions of $Au@Fe_2O_3/SiO_2$ pretreated at 300, 500, or 700 °C are 83%, 32%, and 4%, respectively, when the reaction temperature is −40 °C. Therefore, the specific rates at −40 °C are calculated as 0.46, 0.18, and 0.02 mol g_{Au}^{-1} h^{-1}, respectively, decreasing with the increasing of pretreatment temperature.

To understand why the catalytic activity decreased when the $Au@Fe_2O_3/SiO_2$ catalyst was pretreated at 500 or 700 °C, we conducted XRD experiments (Fig. 2). In general, amorphous SiO_2 has a broad feature at 2θ = 22°, and gold peaks appear at 2θ = 38°, 44°, 65°, and 78° [79]. In the XRD pattern of as-synthesized $Au@Fe_2O_3/SiO_2$, one can see very broad features (especially the one at 2θ = 38°) corresponding to metallic gold, and FeO_x species is amorphous or not detected clearly. The peaks corresponding to crystalline Fe_2O_3 become sharper and sharper with the pretreatment temperature. We used a commercial α-Fe_2O_3 to help with the peak assignment, and the XRD peak positions are consistent with the literature data [80]. Meanwhile, the peaks corresponding to metallic

Table 1
EDX results, CO conversions, and specific rates of various catalysts pretreated at different temperatures.

Sample	Au content/wt%	Fe content/wt%	CO conversion at -40 °C/%	Specific rate at -40 °C/mol·g_{Au}^{-1}·h^{-1}
Au@Fe_2O_3-I/SiO_2, 500 °C	3.8	2.7	85	0.41
Au@Fe_2O_3-II/SiO_2, 500 °C	3.3	10.1	32	0.18
Au@Fe_2O_3-III/SiO_2, 500 °C	3.4	27.1	44	0.24
Au@Fe_2O_3-IV/SiO_2, 500 °C	2.5	34.6	23	0.17
Au@Fe_2O_3/SiO_2, 300 °C	3.3	10.3	83	0.46
Au@Fe_2O_3/TiO_2, 300 °C	3.8	10.4	49	0.23
Au@Fe_2O_3/C, 300 °C	3.3	10.1	85	0.47
Au@Fe_2O_3/Fe_2O_3, 300 °C	3.5	54.6	71	0.37
Au@Fe_2O_3, 300 °C	11.7	30.2	54.(12 mg catalyst)	0.35
Au/SiO_2, 500 °C	3.3	-	14	0.08
Au/TiO_2, 300 °C	3.4	-	0	0
Au/C, 300 °C	3.6	-	11	0.06
Au/Fe_2O_3, 300 °C	3.6	52.7	14	0.07

gold also become sharper, indicating the growth of gold nanoparticles when the pretreatment temperature increases. The sintering of gold nanoparticles at high temperatures is illustrated by the TEM data in Fig. 3. This figure compares the catalyst collected after pretreatment at 300 or 700 °C and subsequent reaction testing. Put together, these data indicate that the decrease in activity upon pretreating Au@Fe_2O_3/SiO_2 may be due to the crystallization of Fe_2O_3 and growth of gold nanoparticles. It seems that the Fe_2O_3 shell is not unbreakable at high temperatures. This argument is based on the observation that gold nanoparticles significantly sinter after pretreatment at 700 °C (Fig. 3B).

3.2. *Au@Fe_2O_3/SiO_2: effect of shell thickness*

To begin with, Au@Fe_2O_3 samples with different Fe contents were made by adjusting the amounts of $Fe(CO)_5$ precursor and oleylamine–oleic acid mixture used, as specified in Section 2. The Au and Fe contents of each sample were measured by EDX and listed in Table 1. The gold loading decreases slightly and the Fe content increases obviously when more $Fe(CO)_5$ precursor is used, implying the increase of shell thickness. Knowing the contents and densities of Au and Fe_2O_3 as well as the average diameter of gold nanoparticles (2.5 nm, as estimated by TEM), we did calculations and estimated that the Fe_2O_3 shell thicknesses of Au@Fe_2O_3-I, Au@Fe_2O_3-II, Au@Fe_2O_3-III, and Au@Fe_2O_3-IV samples are roughly 1, 2, 3, and 4 nm, respectively (see Supporting Information). There are several assumptions for calculation: (1) both gold nanoparticles and Au@Fe_2O_3 structures are spherical; (2) the Fe_2O_3 shell is in close contact with the gold core; (3) the coating of Fe_2O_3 on gold nanoparticle is uniform; (4) there is no separate Fe_2O_3 phase. These assumptions are valid, as exemplified by the HAADF images in Fig. 4. These images show the morphologies of as-synthesized Au@Fe_2O_3-II and Au@Fe_2O_3-IV. The thicknesses of the Fe_2O_3 shells are estimated as 2 and 4 nm, respectively.

Fig. 5 shows the light-off curves of Au@Fe_2O_3/SiO_2 catalysts with different Fe_2O_3 shell thickness. These catalysts were all pretreated at 500 °C. The activity generally decreases with the thickness of the Fe_2O_3 shell (T_{50} = −52, −28, −39, and −24 °C, respectively), although all of these catalysts show significant conversions below 0 °C. To compare the activity more quantitatively, specific rates were calculated (Table 1). For instance, the CO conversions of Au@Fe_2O_3-I/SiO_2 (3.8 wt% Au), Au@Fe_2O_3-II/SiO_2 (3.3 wt% Au), Au@Fe_2O_3-III/SiO_2 (3.4 wt% Au), and Au@Fe_2O_3-IV/SiO_2 (2.5 wt% Au) at −40 °C are 85%, 32%, 44%, and 23%, respectively. Therefore, the specific rates at −40 °C are calculated as 0.41, 0.18, 0.24, and 0.17 mol g_{Au}^{-1} h^{-1}, respectively, generally decreasing with the increasing of thickness of the Fe_2O_3 shell. However, the activity is still higher than that on 500 °C-pretreated Au/SiO_2 (3.3 wt% Au) without any Fe_2O_3 shell. The latter catalyst was made by depositing gold nanoparticles on a commercial SiO_2 support. Au/SiO_2 shows 14% conversion at −40 °C, corresponding to a specific rate of 0.08 mol g_{Au}^{-1} h^{-1}.

Fig. 6 shows the XRD data of Au@Fe_2O_3/SiO_2 catalysts collected after pretreatment at 500 °C and subsequent reaction testing. The peaks corresponding to crystalline Fe_2O_3 increase with the content of Fe. This indicates that too much Fe would lead to the crystallization of Fe_2O_3 more obviously and perhaps block some active sites within the shell.

Fig. 7 shows the TEM data of Au@Fe_2O_3 structures at various stages of preparation and treatment. For as-prepared Au@Fe_2O_3, the gold nanoparticles are uniform and the Fe_2O_3 shells are relatively uniform, too. Going from Fig. 7A to B, the shell thickness increases with the amount of Fe in the samples (10.1 and 34.6 wt%, respectively). When deposited onto SiO_2 support, some of the shell

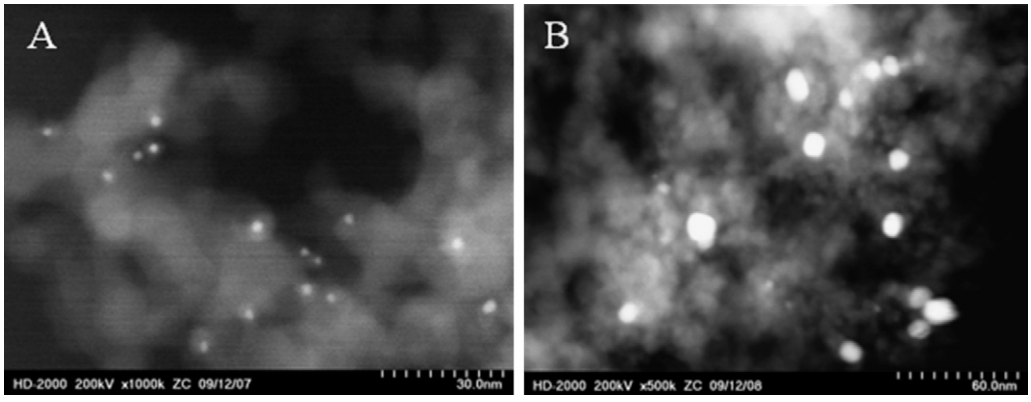

Fig. 3. Dark-field TEM images. (A) Au@Fe_2O_3/SiO_2 pretreated at 300 °C and subjected to reaction testing and (B) Au@Fe_2O_3/SiO_2 pretreated at 700 °C and subjected to reaction testing. The thickness of the original Fe_2O_3 shell was estimated to be 2 nm. The scale bars represent 30 nm (A) and 60 nm (B), respectively.

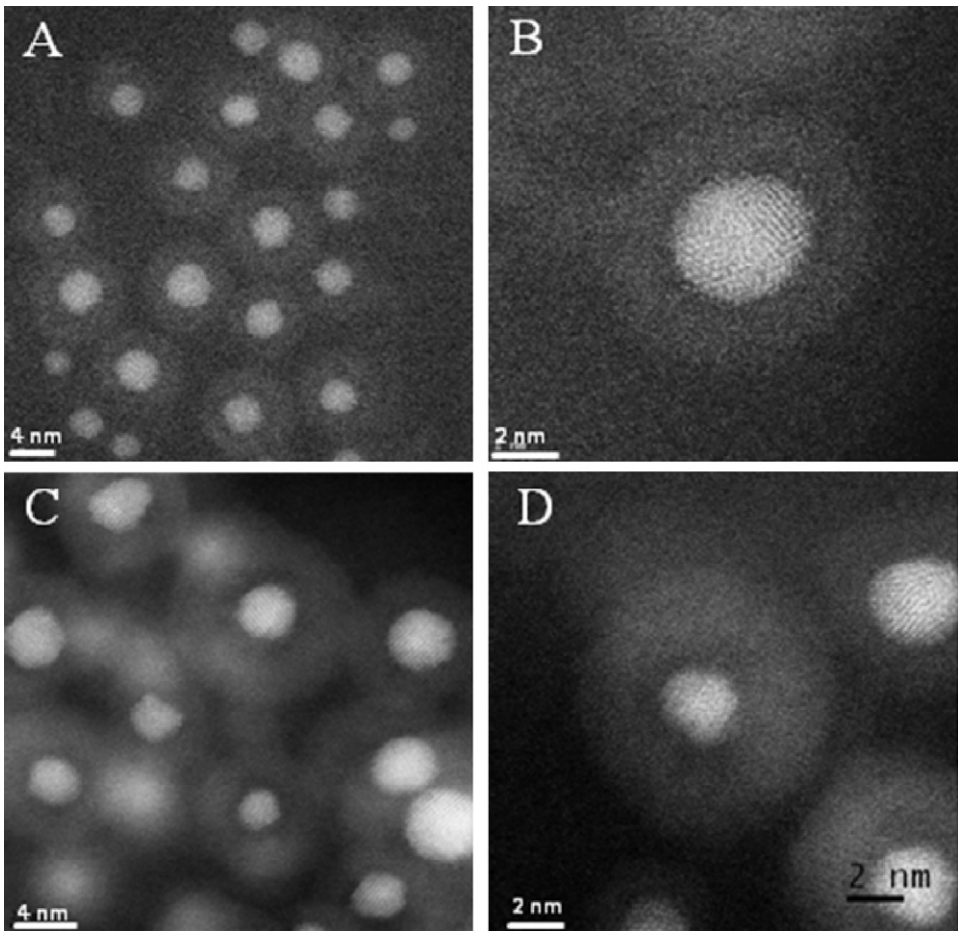

Fig. 4. HAADF images of as-synthesized Au@Fe_2O_3-II (A and B) and Au@Fe_2O_3-IV (C and D).

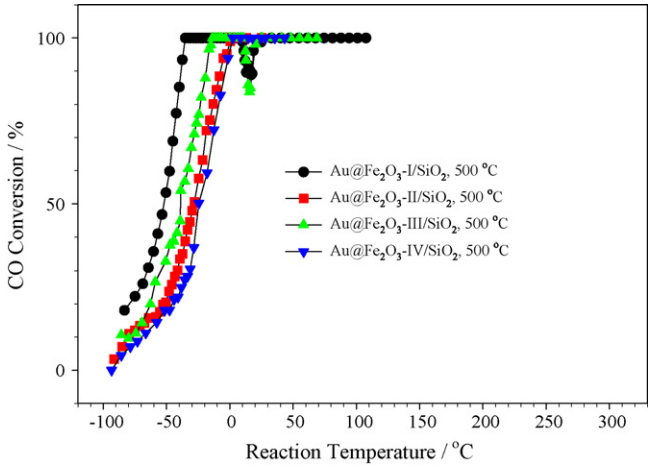

Fig. 5. CO conversions on 500 °C-pretreated Au@Fe_2O_3/SiO_2 catalysts with different original Fe_2O_3 shell thickness (estimated as 1, 2, 3, and 4 nm).

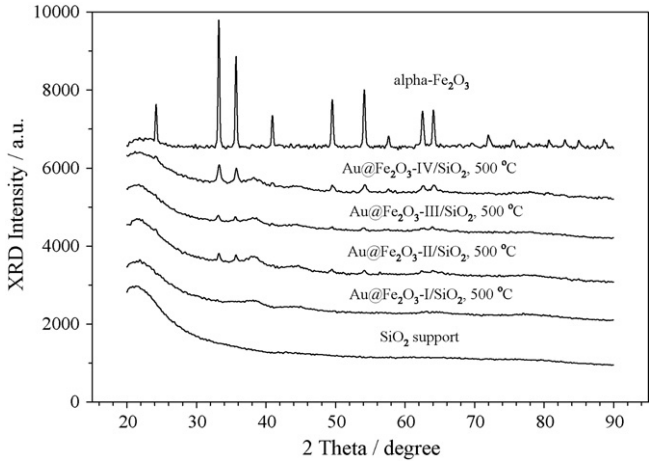

Fig. 6. XRD patterns of Au@ Fe_2O_3/SiO_2 catalysts collected after pretreatment at 500 °C and reaction testing. The thicknesses of original Fe_2O_3 shells were estimated as 1, 2, 3, and 4 nm, respectively.

structures are not clear due to insufficient contrast between the support and Fe_2O_3. However, one still can see the presence of core–shell structures on support surfaces. After the pretreatment of these catalysts at 500 °C and subsequent reaction testing, the core–shell structures are still present.

To further confirm the presence of core–shell structures, we conducted HAADF characterization of spent Au@Fe_2O_3-II/SiO_2 and Au@Fe_2O_3-IV/SiO_2 catalysts collected after pretreatment at 500 °C and subsequent reaction testing. As shown in Fig. 8, the core–shell structures are still present. However, sometimes the shells become rough and the gold nanoparticles are not exactly at the center of the shells after pretreatment at 500 °C and subsequent reaction testing (Fig. S2), indicating the instability of the core–shell structures at elevated temperatures. This state may be a precursor or transition state for the breakage of the shell and sever sintering of gold nanoparticles at 700 °C (Fig. 3).

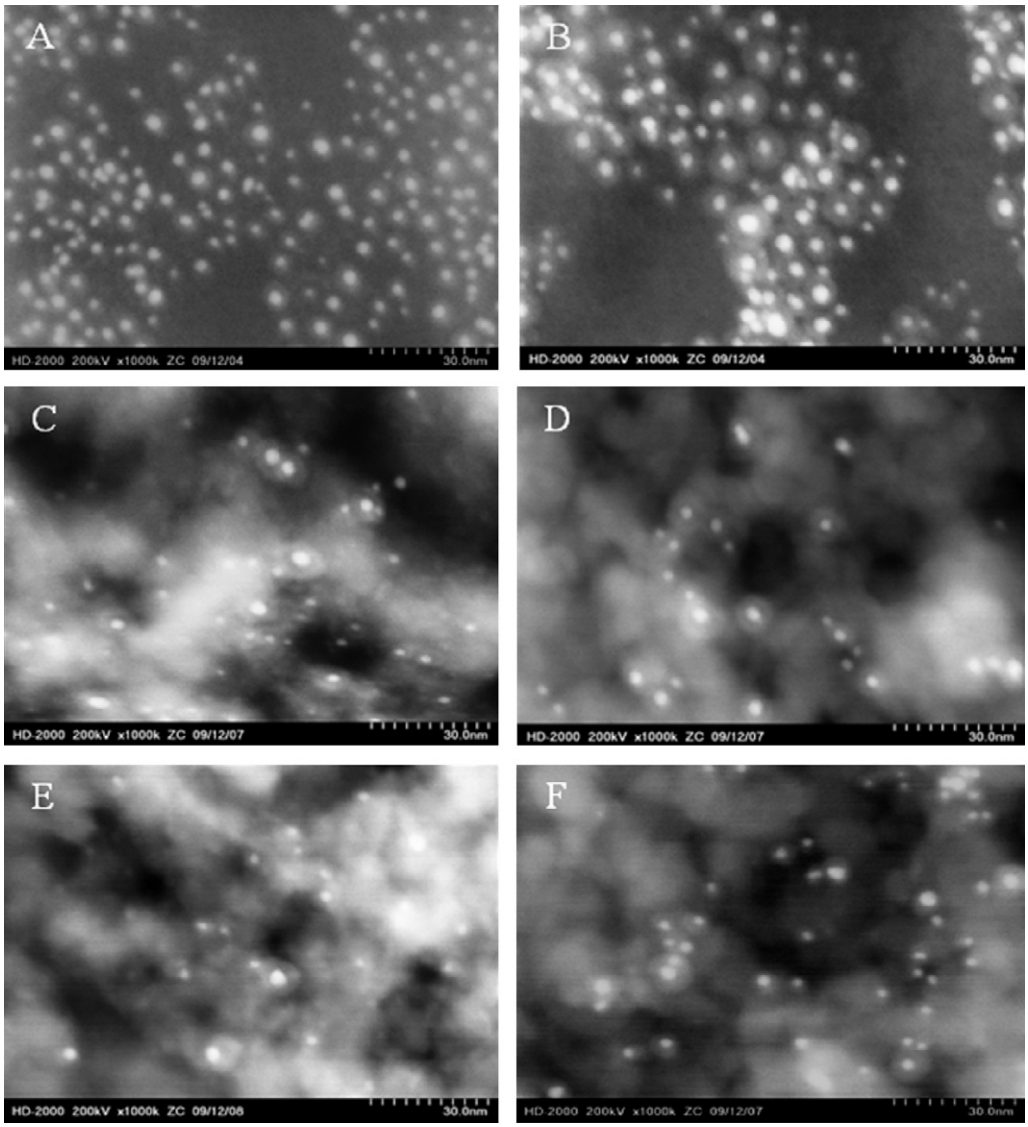

Fig. 7. TEM images of (A) as-prepared Au@Fe_2O_3-II, (B) as-prepared Au@Fe_2O_3-IV, (C) as-prepared Au@Fe_2O_3-II/SiO_2, (D) as-prepared Au@Fe_2O_3-IV/SiO_2, (E) Au@Fe_2O_3-II/SiO_2 collected after pretreatment at 500 °C and reaction testing, and (F) Au@Fe_2O_3-IV/SiO_2 collected after pretreatment at 500 °C and reaction testing. The scale bars represent 30 nm consistently.

3.3. *Effect of different supports*

Above, we have used SiO_2 as the support for loading Au@Fe_2O_3 core–shell structures. It is known that solid supports are generally used to provide high surface area for metal dispersion as well as specific interaction between active metal and support surface to enhance catalytic performance. Therefore, we also used commercial TiO_2, C, and Fe_2O_3 supports to test the effect of different supports, and the shell thickness of Au@Fe_2O_3 is chosen to be 2 nm. These supported catalysts were all pretreated at 300 °C prior to reaction testing. As shown in Fig. 9, the conversion curves are similar to each other in terms of shapes and positions, except that the conversions on Au@Fe_2O_3/TiO_2 are lower. The T_{50} values of 300 °C-pretreated Au@Fe_2O_3/SiO_2, Au@Fe_2O_3/TiO_2, Au@Fe_2O_3/C, and Au@Fe_2O_3/Fe_2O_3 are −55, −39, −58, and −51 °C, respectively. The specific rates of these catalysts at −40 °C are calculated as 0.46, 0.23, 0.47, and 0.37 mol g_{Au}^{-1} h^{-1}, respectively. Noteworthy is that 300 °C-pretreated Au@Fe_2O_3 (12 mg instead of a regular load of 50 mg due to high CO conversion) itself shows significant CO conversion below 0 °C, and its specific rate at −40 °C is calculated as 0.35 mol g_{Au}^{-1} h^{-1}. The plateau in the conversion curve may be due to the deactivation of catalyst during the course of measuring the conversion curve. Although unsupported Au@Fe_2O_3 itself shows significant CO conversion and the advantage of support in this matter is not particularly eminent, we believe that these supported Au@Fe_2O_3 may find better performance in other catalytic reactions where the acid–base or redox properties of the supports matter.

The effect of high-temperature pretreatment on the activity of Au@Fe_2O_3/TiO_2 was studied. As shown in Fig. 10, the CO conversions decrease sharply when calcining Au@Fe_2O_3/TiO_2 at 700 °C, and the behavior observed here is more severe than that observed in Au@Fe_2O_3/SiO_2 system (Fig. 1). XRD data show the growth of gold nanoparticles, but the crystallization of amorphous Fe_2O_3 is not obvious (Fig. S3). TEM data clearly show that the sintering of gold nanoparticles upon pretreatment at 700 °C (Fig. 11). Therefore, it is possible for the breakage of the Fe_2O_3 shells and growth of gold nanoparticles at elevated temperatures at 700 °C. Xu and co-workers found that a small portion of gold nanoparticles in Au@SiO_2 escape from the SiO_2 shells to form big agglomerates after conducting the hydrolysis of ammonia borane at 18 °C [48].

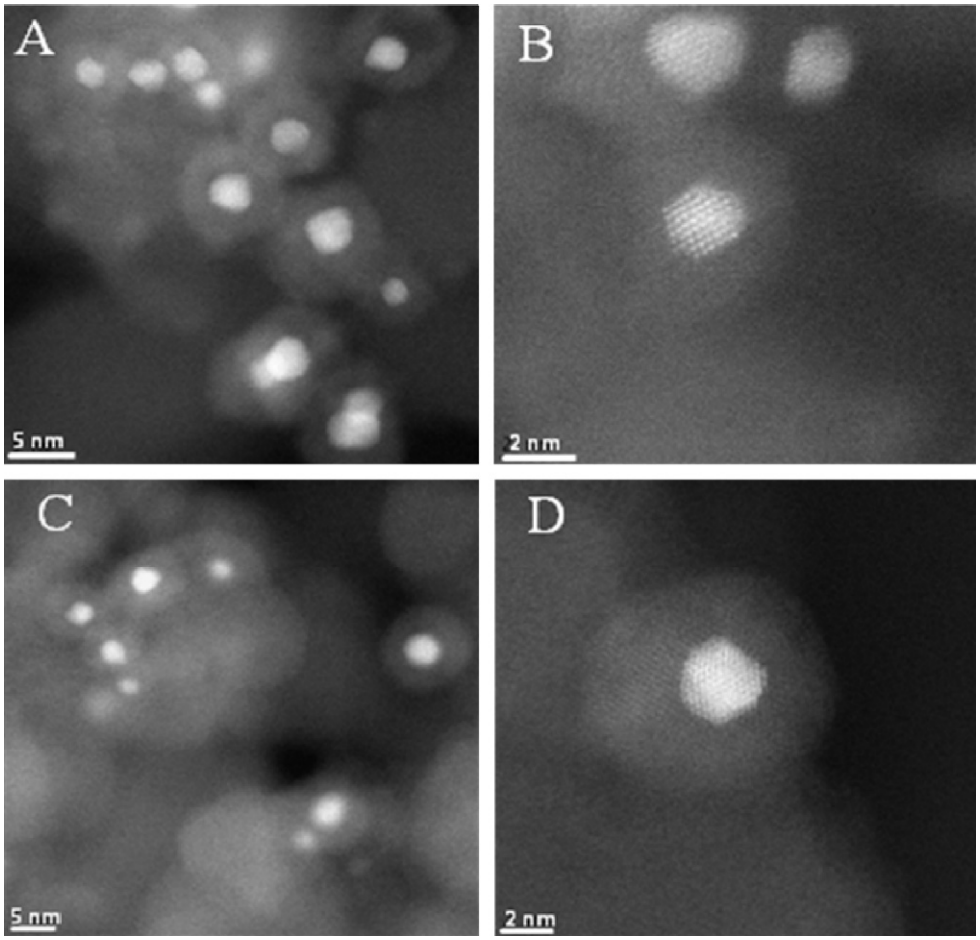

Fig. 8. HAADF images of 500 °C-pretreated Au@Fe_2O_3-II/SiO_2 (A and B) and 500 °C-pretreated Au@Fe_2O_3-IV/SiO_2 (C and D).

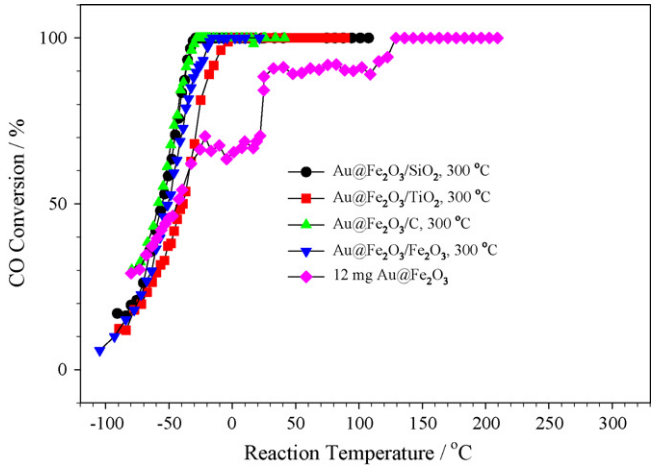

Fig. 9. CO conversions on Au@Fe_2O_3 core–shell structures supported on different solid supports. The thickness of the original Fe_2O_3 shell was estimated to be 2 nm.

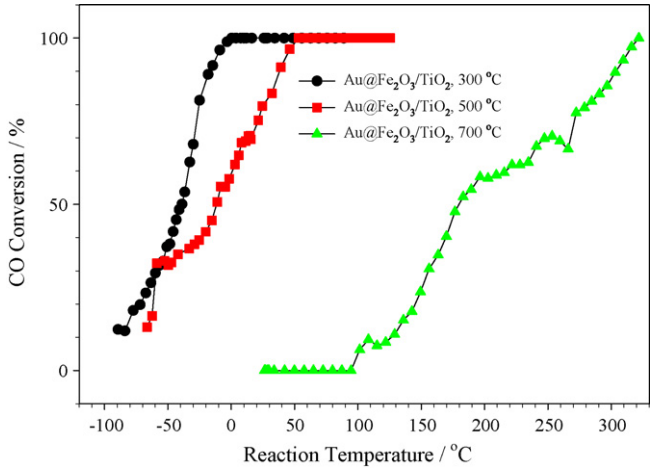

Fig. 10. CO conversions on Au@Fe_2O_3/TiO_2 pretreated at different temperatures (300, 500, or 700 °C). The thickness of the original Fe_2O_3 shell was estimated to be 2 nm.

3.4. Control experiments

To put our results in better perspective, we compared the supported core–shell catalysts with regular supported catalysts prepared by depositing gold colloids on commercial supports. As shown in Fig. 12, Au/SiO_2 shows very low activity when pretreated at 300 °C, possibly because such a temperature is not high enough to burn off organic species. This is proven by the TG/DTG data (Fig. S4). To activate the catalyst, we pretreated Au/SiO_2 at 500 °C. The TG/DTG data in Fig. S4 show that oxidative pretreatment at 500 °C is sufficient to remove most organic species. The 500 °C-pretreated Au/SiO_2 is active below 0 °C, but it is still less active than Au@Fe_2O_3/SiO_2 with a comparable gold loading (Table 1). The presence of Fe_2O_3 shell could enhance the activity because Au–Fe_2O_3 interface is known to be active for CO oxidation [61–67]. Similarly, Au@Fe_2O_3/TiO_2 is more active than Au/TiO_2, and Au@Fe_2O_3/C is more active than Au/C. More interestingly, Au@Fe_2O_3/SiO_2,

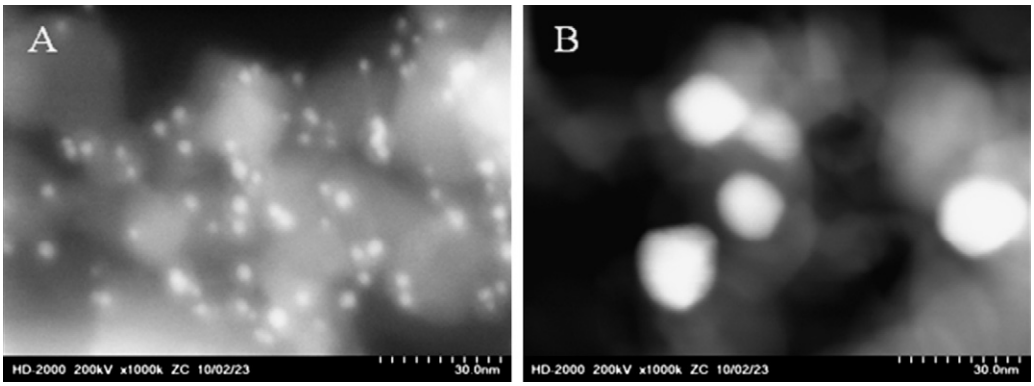

Fig. 11. Dark-field TEM images. (A) Au@Fe_2O_3/TiO_2 collected after pretreatment at 300 °C and reaction testing; (B) Au@Fe_2O_3/TiO_2 collected after pretreatment at 700 °C and reaction testing. The thickness of the original Fe_2O_3 shell was estimated to be 2 nm. The scale bars represent 30 nm consistently.

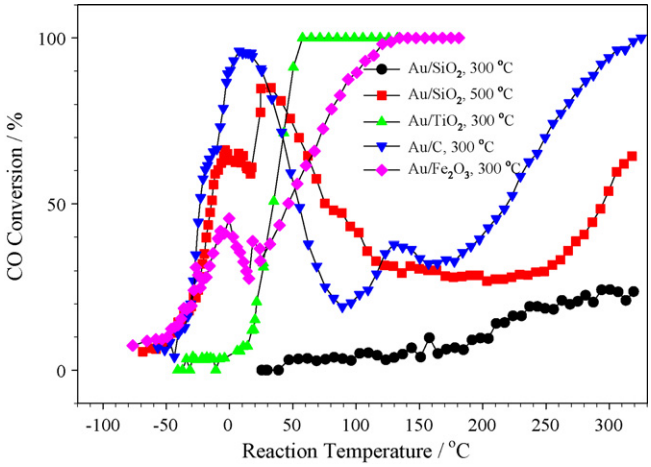

Fig. 12. CO conversions of dodecanethiol-capped Au nanoparticles on different solid supports. These catalysts were pretreated at specified temperatures before reaction testing.

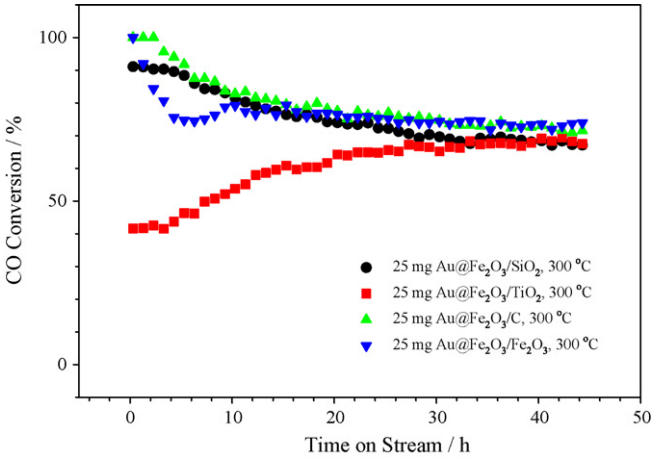

Fig. 13. CO conversions on Au@Fe_2O_3/support catalysts as a function of time on stream. These catalysts were pretreated at 300 °C, and the amount of catalyst was 25 mg. The reaction was carried out at room temperature.

Au@Fe_2O_3/TiO_2, and Au@Fe_2O_3/C catalysts are more active than Au/Fe_2O_3 prepared by dispersing gold nanoparticles on commercial Fe_2O_3. We made the conclusion by comparing the position of CO conversion curves directly because these catalysts have similar gold loadings. The same conclusion is reached if the activity is expressed in terms of specific rates (Table 1). Our data indicate that the interfacial structure between gold nanoparticle and the oxide in contact with gold matters [60,67]. There could be more active sites when gold nanoparticles are surrounded by Fe_2O_3 shells, whereas there could be less active sites when gold nanoparticles are dispersed on less-curved regular Fe_2O_3 support.

3.5. Stability as a function of time on stream

Stability of catalysts is important in practical terms. To test the stability properly, we put 25 mg (instead of the regular load of 50 mg) catalyst in the reactor, in order to make sure that the conversion is not always 100% on stream. The reaction was carried out at room temperature. As shown in Fig. 13, there is some deactivation for 300 °C-pretreated Au@Fe_2O_3/SiO_2, Au@Fe_2O_3/C, and Au@Fe_2O_3/Fe_2O_3 in the initial stage, and the CO conversion then becomes stable after 20 h on stream. For comparison, the CO conversion on Au@Fe_2O_3/TiO_2 increases in the initial stage and then becomes stable after 20 h on stream, in a way similar to that observed with K_2MnO_4/Au/TiO_2 catalyst [70]. The deactivation of gold catalysts during the course of CO oxidation is often ascribed to the accumulation of carbonate and/or formate species [81–85], whereas the increase in CO conversion before reaching a steady state [79,86–91] is ascribed to the accumulation of trace amount of water that promotes CO oxidation and the more sufficient reduction of gold during CO oxidation [89–91]. In our case, although the exact reasons for the catalyst deactivation and activation are not quite clear, we note that the catalytic activity is stable after 20 h on stream.

4. Conclusions

Au@Fe_2O_3 core–shell heterostructures were deposited on SiO_2, TiO_2, C, and Fe_2O_3 supports by colloidal deposition, and the performance in CO oxidation was studied. It is necessary to pretreat the catalysts at elevated temperatures such as 300 °C, in order to remove residual organic species. The burning of organic species could result in the creation of pores for the entrance of CO and O_2 while allowing for the exit of CO_2. However, the catalytic activity decreases further when the pretreatment temperature is 700 °C due to the sintering of gold nanoparticles and the structural changes of the Fe_2O_3 shells. Au@Fe_2O_3/SiO_2 is more active than Au/SiO_2, but the activity generally decreases with the shell thickness. Au@Fe_2O_3/TiO_2, Au@Fe_2O_3/C, and Au@Fe_2O_3/Fe_2O_3 catalysts are also more active than colloidal-deposition-derived Au/TiO_2, Au/C, Au/Fe_2O_3, respectively. The supported Au@Fe_2O_3 catalysts are stable in CO oxidation at room temperature after 20 h on stream. This work illustrates a case study on the use of core–shell structures for making new gold catalysts. Although here we use Fe_2O_3

shell as an example, we believe that this preparation method can be extended to the preparation of new gold catalysts with other shells. Further study may be carried out to study the nature of active sites [92,93] and reaction mechanism using in situ infrared spectroscopy and X-ray absorption.

Acknowledgements

Research sponsored by the Division of Chemical Sciences, Office of Basic Energy Sciences, U.S. Department of Energy under contract DE-AC05-00OR22725 with Oak Ridge National Laboratory, managed and operated by UT-Battelle, LLC. This research was also supported by the appointment for H.F. Yin to the ORNL Research Associates Program, administered by Oak Ridge Associated Universities.

Appendix A. Supplementary data

Supplementary data associated with this article can be found, in the online version, at doi:10.1016/j.cattod.2010.05.013.

References

[1] M. Haruta, M. Daté, Appl. Catal. A 222 (2001) 427.
[2] T.V. Choudhary, D.W. Goodman, Top. Catal. 21 (2002) 25.
[3] A.S.K. Hashmi, G.J. Hutchings, Angew. Chem. Int. Ed. 45 (2006) 7896.
[4] G.C. Bond, C. Louis, D.T. Thompson, Catalysis by Gold, Imperial College Press, London, 2006.
[5] M.C. Kung, R.J. Davis, H.H. Kung, J. Phys. Chem. C 111 (2007) 11767.
[6] C. Della Pina, E. Falletta, L. Prati, M. Rossi, Chem. Soc. Rev. 37 (2008) 2077.
[7] A. Corma, H. Garcia, Chem. Soc. Rev. 37 (2008) 2096.
[8] J.C. Fierro-Gonzalez, B.C. Gates, Chem. Soc. Rev. 37 (2008) 2127.
[9] S. Tsubota, T. Nakamura, K. Tanaka, M. Haruta, Catal. Lett. 56 (1998) 131.
[10] J.D. Grunwaldt, C. Kiener, C. Wogerbauer, A. Baiker, J. Catal. 181 (1999) 223.
[11] F. Porta, L. Prati, M. Rossi, S. Coluccia, G. Martra, Catal. Today 61 (2000) 165.
[12] G. Martra, L. Prati, C. Manfredotti, S. Biella, M. Rossi, S. Coluccia, J. Phys. Chem. B 107 (2003) 5453.
[13] J. Chou, N.R. Franklin, S.-H. Baeck, T.F. Jaramillo, E.W. McFarland, Catal. Lett. 95 (2004) 107.
[14] M. Comotti, W.C. Li, B. Spliethoff, F. Schüth, J. Am. Chem. Soc. 128 (2006) 917.
[15] N.F. Zheng, G.D. Stucky, J. Am. Chem. Soc. 128 (2006) 14278.
[16] N. Hickey, P.A. Larochette, C. Gentilini, L. Sordelli, L. Olivi, S. Polizzi, T. Montini, P. Fornasiero, L. Pasquato, M. Graziani, Chem. Mater. 19 (2007) 650.
[17] Y.M. Liu, H. Tsunoyama, T. Akita, T. Tsukuda, J. Phys. Chem. C 113 (2009) 13457.
[18] Y. Tai, W. Yamaguchi, M. Okada, F. Ohashi, K. Shimizu, A. Satsuma, K. Koji, H. Kageyama, J. Catal. 270 (2010) 234.
[19] A. Quintanilla, V.C.L. Butselaar-Orthlieb, C. Kwakernaak, W.G. Sloof, M.T. Kreutzer, F. Kapteijn, J. Catal. 271 (2010) 104.
[20] W.F. Yan, B. Chen, S.M. Mahurin, E.W. Hagaman, S. Dai, S.H. Overbury, J. Phys. Chem. B 108 (2004) 2793.
[21] W.F. Yan, S.M. Mahurin, B. Chen, S.H. Overbury, S. Dai, J. Phys. Chem. B 109 (2005) 15489.
[22] W.F. Yan, S.M. Mahurin, Z.W. Pan, S.H. Overbury, S. Dai, J. Am. Chem. Soc. 127 (2005) 10480.
[23] A.C. Gluhoi, N. Bogdanchikova, B.E. Nieuwenhuys, J. Catal. 229 (2005) 154.
[24] A. Horváth, A. Beck, A. Sárkány, G. Stefler, Z. Varga, O. Geszti, L. Tóth, L. Guczi, J. Phys. Chem. B 110 (2006) 15417.
[25] Z. Ma, S.H. Overbury, S. Dai, J. Mol. Catal. A 273 (2007) 186.
[26] K. Qian, W.X. Huang, Z.Q. Jiang, H.X. Sun, J. Catal. 248 (2007) 137.
[27] J.P. Ge, Q. Zhang, T.R. Zhang, Y.D. Yin, Angew. Chem. Int. Ed. 47 (2008) 8924.
[28] B.H. Wu, H. Zhang, C. Chen, S.C. Lin, N.F. Zheng, Nano Res. 2 (2009) 975.
[29] S. Albonetti, R. Bonelli, R. Delaigle, C. Femoni, E.M. Gaigneaux, V. Morandi, L. Ortolani, C. Tiozzo, S. Zacchini, F. Trifirò, Appl. Catal. A 372 (2010) 138.
[30] C.L. Peza-Ledesma, L. Escamilla-Perea, R. Nava, B. Pawelec, J.L.G. Fierro, Appl. Catal. A 375 (2010) 37.
[31] H.F. Yin, C. Wang, H.G. Zhu, S.H. Overbury, S.H. Sun, S. Dai, Chem. Commun. (2008) 4357.
[32] S.H. Zhou, H.F. Yin, V. Schwartz, Z.L. Wu, D.R. Mullins, B. Eichhorn, S.H. Overbury, S. Dai, Chem. Phys. Chem. 9 (2008) 2475.
[33] S.H. Zhou, Z. Ma, H.F. Yin, Z.L. Wu, B. Eichhorn, S.H. Overbury, S. Dai, J. Phys. Chem. C 113 (2009) 5758.
[34] E.V. Shevchenko, M.I. Bodnarchuk, M.V. Kovalenko, D.V. Talapin, R.K. Smith, S. Aloni, W. Heiss, A.P. Alivisatos, Adv. Mater. 20 (2008) 4323.
[35] L.M. Liz-Marzan, M. Giersig, P. Mulvaney, Langmuir 12 (1996) 4329.
[36] L.M. Liz-Marzan, P. Mulvaney, J. Phys. Chem. B 107 (2003) 7312.
[37] I. Pastoriza-Santos, J. Perez-Juste, L.M. Liz-Marzan, Chem. Mater. 18 (2006) 2465.
[38] M. Casavola, R. Buonsanti, G. Caputo, P.D. Cozzoli, Eur. J. Inorg. Chem. (2008) 837.
[39] S.H. Liu, M.Y. Han, Chem. Asian J. 5 (2010) 36.
[40] M. Ikeda, T. Tago, M. Kishida, K. Wakabayashi, Chem. Commun. (2001) 2512.
[41] Y.D. Yin, R.M. Rioux, C.K. Erdonmez, S. Hughes, G.A. Somorjai, A.P. Alivisatos, Science 304 (2004) 711.
[42] S. Takenaka, K. Hori, H. Matsune, M. Kishida, Chem. Lett. 34 (2005) 1594.
[43] C.M.Y. Yeung, K.M.K. Yu, Q.J. Fu, D. Thompsett, M.I. Petch, S.C. Tsang, J. Am. Chem. Soc. 127 (2005) 18010.
[44] C.M.Y. Yeung, F. Meunier, R. Burch, D. Thompsett, S.C. Tsang, J. Phys. Chem. B 110 (2006) 8540.
[45] S. Takenka, H. Umebayashi, E. Tanabe, H. Matsune, M. Kishida, J. Catal. 245 (2007) 392.
[46] J.N. Park, A.J. Forman, W. Tang, J.H. Cheng, Y.-S. Hu, H.F. Lin, E.W. McFarland, Small 4 (2008) 1694.
[47] S.H. Joo, J.Y. Park, C.-K. Tsung, Y. Yamada, P.D. Yang, G.A. Somorjai, Nat. Mater. 8 (2009) 126.
[48] H.-L. Jiang, T. Umegaki, T. Akita, X.-B. Zhang, M. Haruta, Q. Xu, Chem. Eur. J. 16 (2010) 3132.
[49] C.M.Y. Yeung, S.C. Tsang, J. Mol. Catal. A 322 (2010) 17.
[50] K.M.K. Yu, C.M.Y. Yeung, D. Thompsett, S.C. Tsang, J. Phys. Chem. B 107 (2003) 4515.
[51] K.M.K. Yu, D. Thompsett, S.C. Tsang, Chem. Commun. (2003) 1522.
[52] T.S.A. Kong, K.M.K. Yu, S.C. Tsang, J. Nanosci. Nanotechnol. 6 (2006) 1167.
[53] Z. Ma, S. Dai, Mater. Technol. 21 (2008) 81.
[54] L. De Rogatis, M. Cargnello, V. Gombac, B. Lorenzut, T. Montini, P. Fornasiero, Chem. Sus. Chem. 3 (2010) 24.
[55] P.M. Arnal, M. Comotti, F. Schüth, Angew. Chem. Int. Ed. 45 (2006) 8224.
[56] J. Lee, J.C. Park, H. Song, Adv. Mater. 20 (2008) 1523.
[57] X.Q. Huang, C.Y. Guo, J.Q. Zuo, N.F. Zheng, G.D. Stucky, Small 5 (2009) 361.
[58] R. Güttel, M. Paul, F. Schüth, Chem. Commun. 46 (2010) 895.
[59] G. Budroni, A. Corma, Angew. Chem. Int. Ed. 45 (2006) 3328.
[60] K. Yu, Z.C. Wu, Q.R. Zhao, B.X. Li, Y. Xie, J. Phys. Chem. C 112 (2008) 2244.
[61] M. Haruta, S. Tsubota, T. Kobayashi, H. Kageyama, M.J. Genet, B. Delmon, J. Catal. 144 (1993) 175.
[62] A.P. Kozlova, S. Sugiyama, A.I. Kozlov, K. Asakura, Y. Iwasawa, J. Catal. 176 (1998) 426.
[63] G.Y. Wang, H.L. Lian, W.X. Zhang, D.Z. Jiang, T.H. Wu, Kinet. Catal. 43 (2002) 433.
[64] S.T. Daniells, A.R. Overweg, M. Makkee, J.A. Moulijn, J. Catal. 230 (2005) 52.
[65] M. Khoudiakov, M.C. Gupta, S. Deevi, Appl. Catal. A 291 (2005) 151.
[66] G.J. Hutchings, M.S. Hall, A.F. Carley, P. Landon, B.E. Solsona, C.J. Kiely, A. Herzing, M. Makkee, J.A. Moulijn, A. Overweg, J. Catal. 242 (2006) 71.
[67] Z.Y. Zhong, J. Ho, J. Teo, S.C. Shen, A. Gedanken, Chem. Mater. 19 (2008) 4776.
[68] M. Brust, M. Walker, D. Bethell, D.J. Schiffrin, R. Whyman, J. Chem. Soc. – Chem. Commun. (1994) 801.
[69] M.J. Hostetler, J.E. Wingate, C.J. Zhong, J.E. Harris, R.W. Vachet, M.R. Clark, J.D. Londono, S.J. Green, J.J. Stokes, G.D. Wignall, G.L. Glish, M.D. Porter, N.D. Evans, R.W. Murray, Langmuir 14 (1998) 17.
[70] H.F. Yin, Z. Ma, M.F. Chi, S. Dai, Catal. Lett. 136 (2010) 209.
[71] E.V. Shevchenko, M.I. Bodnarchitk, M.V. Kovalenko, D.V. Talapin, R.K. Smith, S. Aloni, W. Heiss, A.P. Alivisatos, Adv. Mater. 20 (2008) 4323.
[72] W.C. Li, M. Comotti, F. Schüth, J. Catal. 237 (2006) 190.
[73] Y.Z. Yuan, K. Asakura, H.L. Wan, K. Tsai, Y. Iwasawa, Catal. Lett. 42 (1996) 15.
[74] T.V. Choudhary, C. Sivadinarayana, C.C. Chusuei, A.K. Datye, J.P. Fackler, D.W. Goodman, J. Catal. 207 (2002) 247.
[75] S.-H. Wu, X.-C. Zheng, S.-R. Wang, D.-Z. Han, W.-P. Huang, S.-M. Zhang, Catal. Lett. 96 (2004) 49.
[76] Z. Yan, S. Chinta, A.A. Mohamed, J.P. Fackler, D.W. Goodman, Catal. Lett. 111 (2006) 15.
[77] L.D. Menard, F.T. Xu, R.G. Nuzzo, J.C. Yang, J. Catal. 243 (2006) 64.
[78] C.-W. Chiang, A.Q. Wang, C.-Y. Mou, Catal. Today 117 (2006) 220.
[79] H.G. Zhu, Z. Ma, J.C. Clark, Z.W. Pan, S.H. Overbury, S. Dai, Appl. Catal. A 326 (2007) 89.
[80] G. Shirane, S.J. Pickart, R. Nathans, Y. Ishikawa, J. Phys. Chem. Solids 10 (1959) 35.
[81] A. Knell, P. Barnickel, A. Baiker, A. Wokaun, J. Catal 137 (1992) 306.
[82] B. Schumacher, V. Plzak, M. Kinne, R.J. Behm, Catal. Lett 89 (2003) 109.
[83] P. Konova, A. Naydenov, C. Venkov, D. Mehandjiev, D. Andreeva, T. Tabakova, J. Mol. Catal. A 213 (2004) 235.
[84] P. Konova, A. Naydenov, T. Tabakova, D. Mehandjiev, Catal. Commun. 5 (2004) 537.
[85] Y. Hao, M. Mihaylov, E. Ivanova, K. Hadjiivanov, H. Knözinger, B.C. Gates, J. Catal. 261 (2009) 137.
[86] M.A.P. Dekkers, M.J. Lippits, B.E. Nieuwenhuys, Catal. Lett. 56 (1998) 195.
[87] E.D. Park, J.S. Lee, J. Catal. 186 (1999) 1.
[88] N.A. Hodge, C.J. Kiely, R. Whyman, M.R.H. Siddiqui, G.J. Hutchings, Q.A. Pankhurst, F.E. Wagner, R.R. Rajaram, S.E. Golunski, Catal. Today 72 (2002) 133.
[89] Z. Ma, H.F. Yin, S.H. Overbury, S. Dai, Catal. Lett. 126 (2008) 20.
[90] Z.L. Wu, S.H. Zhou, H.G. Zhu, S. Dai, S.H. Overbury, Chem. Commun. (2008) 3308.
[91] Z.L. Wu, S.H. Zhou, H.G. Zhu, S. Dai, S.H. Overbury, J. Phys. Chem. C 113 (2009) 3726.
[92] S. Minicò, S. Scirè, C. Crisafulli, S. Galvagno, Appl. Catal. B 34 (2001) 277.
[93] V.R. Choudhary, V.P. Patil, P. Jana, B.S. Uphade, Appl. Catal. A 350 (2008) 186.